

www.acsami.org Research Article

Cu-Based Bimetallic Catalysts for Electrocatalytic Oxidative Dehydrogenation of Furfural with Practical Rates

Hengzhou Liu, Jiaqi Yu, Yifu Chen, Jungkuk Lee, Wenyu Huang, and Wenzhen Li*



Cite This: https://doi.org/10.1021/acsami.3c06783



ACCESS |

III Metrics & More





ABSTRACT: Electrocatalytic oxidative dehydrogenation (EOD) of aldehydes enables ultra-low voltage, bipolar H_2 production with co-generation of carboxylic acid. Herein, we reported a simple galvanic replacement method to prepare CuM (M = Pt, Pd, Au, and Ag) bimetallic catalysts to improve the EOD of furfural to reach industrially relevant current densities. The redox potential difference between Cu/Cu^{2+} and a noble metal M/M^{y+} can incorporate the noble metal on the Cu surface and enlarge its surface area. Particularly, dispersing Pt in Cu (CuPt) achieved a record-high current density of 498 mA cm⁻² for bipolar H_2 production at a low cell voltage of 0.6 V and a Faradaic efficiency of >80% to H_2 . Future research is needed to deeply understand the synergistic effects of Cu-M toward EOD of furfural, and improve the Cu-M catalyst stability, thus offering great opportunities for future distributed manufacturing of green hydrogen and carbon chemicals with practical rates and low-carbon footprints.



KEYWORDS: hydrogen, biomass, bimetal, electrocatalytic oxidative dehydrogenation, aldehyde

1. INTRODUCTION

Hydrogen (H₂) is regarded as the best means to store energy generated from intermittent renewable power sources.^{1,2} With a large growing capacity of localized renewable energy sources such as solar and wind energies, the storage system with a similar magnitude is equally important.¹ Coupling renewable electricity with water electrolysis can realize green H₂ production.^{1,3,4} The green H₂ can serve as an ideal sustainable energy carrier and be further converted to meet the energy demands in the industrial and transportation sectors. However, conventional water electrolyzers suffered from high overpotentials, largely because of the sluggish oxygen evolution reaction (OER) on the anode. The high thermodynamic potential of OER ($E^0 = 1.23 \text{ V } vs \text{ SHE}$, at pH = 0) and its slow kinetics, with multiple proton and electron transfer steps included, greatly hampers the overall efficiency of water electrolysis.⁵ Besides, the generation of reactive oxygen species could damage the ion exchange membrane, and the potential mixing of cathodic H₂ (two-electron transfer) and anodic O₂ (four-electron transfer) because of their unbalanced gas pressures could lead to severe safety issues.⁵⁻⁷

One strategy to mitigate the abovementioned problems is to replace OER with an economic oxidation at the anode with more favorable thermodynamics.^{7–9} Recently, Wang *et al.*⁹ and our group¹⁰ reported that Cu-based electrocatalysts can promote a novel electrocatalytic oxidative dehydrogenation (EOD) pathway, through which H₂ and carboxylic acid can be co-generated from aldehyde oxidation (Scheme 1, RXN 1) at anodic potentials near 0 V [*vs* reversible hydrogen electrode (RHE)], and the H atoms in the formation of H₂ are solely

Scheme 1. Comparison of Different Oxidative Transformations of Aldehyde

Electrochemical Faradaic anodic reactions:

 $2R-CHO + 4OH^{-} = 2R-COO^{-} + 2H_{2}O + 2e^{-} + H_{2}(RXN 1)$

 $R-CHO + 3OH- = R-COO- + 2H_2O + 2e^-(RXN 2)$

Non-Faradaic reactions:

 $R-CHO + OH-= R-COO- + H_2(RXN3)$

 $2R-CHO + OH- = R-COO- + R-CH_2OH (RXN 4)$

from the aldehyde group. The newly discovered EOD mechanism is fundamentally different from a few related known reactions, namely the conventional electrocatalytic oxidation (ECO) of aldehydes (Scheme 1, RXN 2),^{11–14} base-/metal-catalyzed oxidation of aldehydes (Scheme 1, RXN 3),^{15–23} and the Cannizzaro disproportionation reaction

(Scheme 1, RXN 4) without H₂ evolution. Compared to RXN 2, EOD is intrinsically more productive from the perspective of atom economy because it utilizes the aldehyde only for the production of H₂, instead of H₂O, and non-noble metal-based catalysts (*i.e.*, Cu and Ag) can be employed to achieve high current density at a significantly lower onset

Received: May 12, 2023 Accepted: July 5, 2023



potential than RXN 2 (i.e., 0.05 V for EOD vs > 1.0 V for ECO). RXN 3 and RXN 4 are chemical transformations that cannot be directly used to replace OER at the anode of electrochemical cells.

Biomass-derived furfural has been selected as a model aldehyde because of its mature production technology and large productivity (~0.43 million tons/year).^{24–26} Coupling the EOD reaction with the cathodic hydrogen evolution reaction (HER) enabled a bipolar H₂ production system (Scheme 2) with ultra-low cell voltages, a double production

Scheme 2. Reaction Equations for Bipolar H₂ Production

Bipolar H2 production system:

Anodic EOD: $2R-CHO + 4OH^- = 2R-COO^- + 2H_2O + 2e^- + H_2$

Cathodic HER: $2H_2O + 2e^- \rightarrow 2OH^- + H_2$

Combined reaction: R-CHO + OH⁻ → R-COO⁻ + H₂

rate of H₂, and the co-production of the carboxylic acid product [*e.g.*, 2-furoic acid (2-FA)] at the anode. Our initial techno-economic analysis (TEA) study based on such a process has shown promising economic viability of H₂ production (*i.e.*, \$2.51/kg of H₂) with co-generation of value-added 2-FA.¹⁰ Although successful process design and indepth mechanistic investigation of reaction pathways among different aldehyde oxidative reactions (Scheme 1, RXN 1-4) were reported in our previous works, ¹⁰ the kinetics of the bipolar H₂ production system are worth a further increase. In such a process, the rate-limiting reaction is the anodic EOD, since the overpotential of cathodic HER on noble metals can be extremely low (*e.g.*, <0.05 V on Pt catalysts at 100 mA cm⁻²²⁷). Therefore, developing efficient anodic catalysts is vital to further enhancing the EOD kinetics and pushing the overall bipolar H₂ production system to practically viable.

In this work, we developed Cu-based electrocatalysts by galvanic replacement methods for EOD and achieved highly selective and active H₂ generation under ultra-low anodic potentials *versus* RHE. The standard potential difference between Cu/Cu^{x+} and M/M^{y+} (M = Ag, Au, Pd, and Pt) as the driving force fully etched the Cu foam substrate and oxidized its surface, resulting in a great increase in the surface roughness. Specifically, dispersing Pt atoms into porous Cu (*i.e.*, CuPt/Cu) delivers the highest RF-normalized partial current density of anodic H₂ (RF-*j*_{A-H₂}) and a maximum *j*_{A-H₂} of 357 mA cm² at 0.4 V_{RHE} among four bimetallic catalysts. More importantly, when implementing this CuPt/Cu catalyst in a zero-gap membrane electrode assembly (MEA)-based flow cell, the high EOD activity enables a bipolar H₂ production to achieve an industrially relevant partial current density of 498 mA.cm⁻² at a low cell voltage of 0.6 V. Such a process allows for Faradaic efficiencies (FES) of both cathodic and anodic H₂

of \sim 100% and a co-generation of 2-FA from the anode.

2. EXPERIMENTAL METHODS

2.1. Materials Synthesis. The copper foam was first sonicated in 2 M HCl solution for 5 min to clean its surface, followed by rinsing and sonicating in DI water. The cleaned Cu foam was then sonicated (RF-power, 90 W; operating frequency, 35 kHz) in 50 mM solutions of the precursor M (Pt, Pd, Au, and Ag) at room temperature for 30 s, to etch the Cu surface, and to exchange M with Cu galvanically, in order to form the CuM/Cu electrode. The precursor solutions containing metal M include HPtCl₄, AuCl₃, Pd(NO₃)₂, and AgNO₃. Finally, the surface copper oxides in CuM/Cu electrodes were *in situ*

electroreduced at $-0.1~V_{RHE}$ for 3 min. The detailed optimization of synthesis conditions was shown in our previous work.¹⁰

The Pt-based electrode was prepared by spray-coating Pt/C (0.5 mg_{Pt} cm⁻²) on an acid-treated carbon cloth substrate. The carbon cloth was first treated in 67–70 wt % HNO₃ at 110 °C for 1 h 45 min to improve its hydrophilicity. The catalyst ink was prepared by dispersing Pt/C particles (10 mg_{Pt} mL⁻¹) in a mixture of DI water,2-propanol, and an anion-exchange ionomer (AS-4) by ultrasonication. The mass ratio of Pt/C and the ionomer was 4:1. The catalyst ink was then air-brushed onto the substrate to reach the final loadings.

2.2. Electrochemical Measurements in the H-Type Cell. To test EOD performances in an H-type cell, a three-electrode cell was set up with a Ag/AgCl reference electrode and a Pt foil counter electrode. Potentiostatic electrochemical impedance spectroscopy (PEIS) was used to measure the resistance between the working and reference electrodes with 90% *IR*-compensation applied for all electrochemical measurements. A Nafion membrane (K⁺ form) was used to separate the anode and cathode compartments, and the working electrode has a geometric area of 1 cm². 1.0 M KOH solution was used for preparing 15 mL electrolyte for each compartment. It is worth mentioning that the as-prepared furfural-containing electrolyte was immediately used to conduct electrochemical tests, in order to avoid its degradation to humins as well as to minimize the side Cannizzaro reaction in the alkaline solution.

Linear sweep voltammetry (LSV) and chronoamperometry (CA) tests were performed with a constant flow of argon (Ar) through the catholyte to deaerate and online analyze the evolved $\rm H_2$ by a GC (SRI 8610C). LSV was conducted at 10 mV s $^{-1}$ without magnetic stirring. During the CA tests, the catholyte and the anolyte were separately stirred by two polytetrafluoroethylene (PTFE)-coated magnetic bars (20 \times 6 mm, Chemglass Life Sciences) at 350 r.p.m. Potentials $\it versus$ RHE were reported; RHE relative to those $\it versus$ Ag/AgCl was calculated by the following equation

$$E_{\text{RHE}} = E_{\text{Ag/AgCl}} + 0.197 \text{ V} + 0.059 \text{ V} \times \text{pH}$$

2.3. Electrochemical Measurements in the MEA-Based Flow **Electrolyzer.** The flow reactor setup and conditions were adopted from our previous works. 10 Specifically, the flow electrolyzer contained two stainless-steel flow-field plates with serpentine channels, PTFE and silicone gaskets, and the MEA composed of two electrodes and a membrane was fabricated after assembling the cell hardware. The catholyte and the anolyte were circulated at 10mL min⁻¹ by a peristaltic pump (Masterflex L/S). To avoid current density exceeding the limit of the potentiostat, we applied a customdesigned flow cell with an active surface area of 1 cm² (1 \times 1 cm²) for the anode and an active surface area of $6.25 \text{ cm}^2 (2.5 \times 2.5 \text{ cm}^2)$ for the cathode. This cell configuration was based on the rate-limiting step of the anodic EOD in the EOD-HER paired system, since HER is much favorable thermodynamically ($E^0 = 0$ vs SHE, at pH = 0) and kinetically (on noble metal Pt/C catalysts). The applied potential or current was well controlled by a potentiostat/galvanostat (Biologic SP-300) with 70% IR-compensation. A piece of anion exchange membrane (Tokuyama A201, ~29 µm) was used to separate the catholyte and the anolyte. All experiments were performed at room temperature.

2.4. Product Analysis. The details of product analysis can be found from our previous work. 10 In brief, the electrolyte was analyzed by a high-performance liquid chromatograph equipped with a variable wavelength detector with the wavelength of 260 nm. The Bio-Rad column (Aminex HPX-87H) was used for analyzing anodic species (including furfural and 2-FA). A C18 HPLC column (Gemini 3 μ m, 110 Å, 100 \times 3 mm) was used to quantify furfuryl alcohol produced from the Cannizzaro reaction. H_2 was quantified by an on-line gas chromatograph equipped with HaySep D and MolSieve 5 Å columns and a thermal conductivity detector. The calibration curve was built by analyzing the standard calibration gases with different concentrations (10–10,000 ppm). The H_2 generation rate was calculated based on the H_2 concentration and the volumetric flow rate of inlet gas, and the total produced H_2 was obtained by integrating the H_2 production rate vs reaction time with polynomial curve fitting. 10

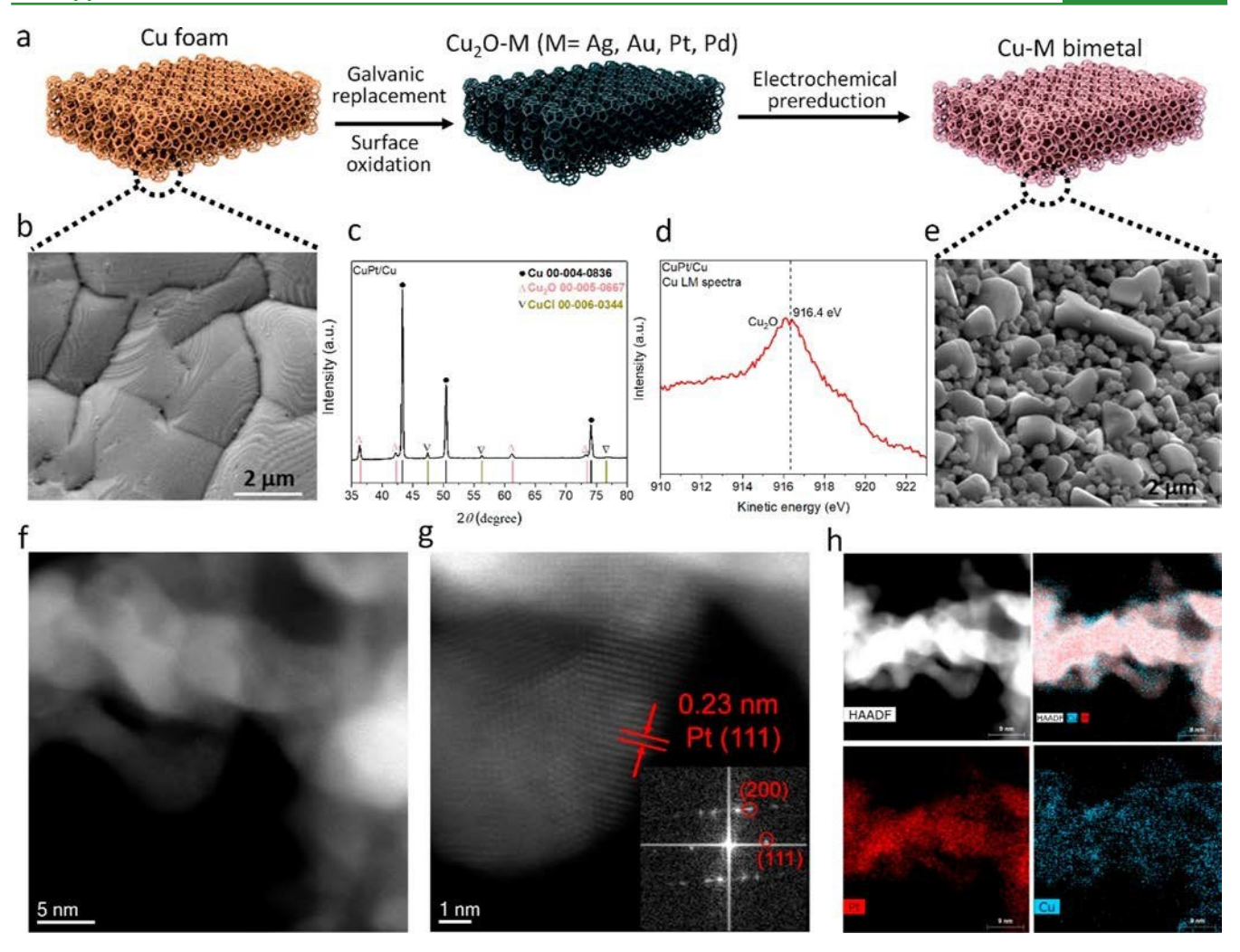


Figure 1. Synthesis and characterization of Cu-based bimetallic catalysts. (a) Scheme of synthesis of Cu-M bimetals by the galvanic replacement method. (b) SEM image of the Cu foam. (c) XRD patterns, (d) Auger Cu LM spectrum, and (e) SEM image of as-synthesized CuPt/Cu. (f) STEM image and (g) HR-STEM image of Cu₂O and Pt regions. The inset image is the FFT pattern. HR-STEM images show the lattice spacing of Pt, which agree with the calculated lattice spacing from FFT. (h) HAADF-STEM EDS elemental mapping, which shows Pt (red color) distributed on a Cu substrate (blue color). It should be noted that because of the close lattice parameters, we cannot simply assign the observed lattice fringe to Cu₂O(111) or Pt(111), and a mixture of Pt with Cu₂O is possible according to the EDS mapping results.

The Faradaic efficiency (FEi) and partial current density of H₂ ($j_{\rm H_2}$) can be calculated using following equations

$$FE_i = \frac{n_i z_i F}{O} \times 100\%$$

$$j_{\rm H_2} = \frac{Q}{t} \times FE$$

where n_i is the moles of product i; z_i is the electron-transfer number for one product molecule; F is the Faraday constant (96,485 C mol⁻¹); Q is the total charge passed through the electrolytic cell; and t is the electrolysis time (s). It should be noted that the 2-FA produced from the EOD pathway was calculated by subtracting 2-FA generated from the Cannizzaro pathway (through quantifying furfuryl alcohol) from the total quantified 2-FA.

2.5. Materials Characterization. 2.5.1. Physical Characterization. X-ray diffraction (XRD) crystallography was performed on a X-ray diffractometer (Siemens D500, Cu K α source, $\lambda = 1.5432$ Å) with a tube voltage of 45 kV and a tube current of 30 mA. The scan was carried out at a rate of 10° min⁻¹ and a step size of 0.02°. X-ray photoelectron spectroscopy (XPS) was performed on an X-ray photoelectron spectrometer (Kratos Amicus/ESCA 3400, with Mg K α X-rays, 1253.7 eV). All XPS spectra were calibrated with the C 1s

peak at 284.8 eV. Scanning electron microscopy-energy-dispersive X-ray spectroscopy (SEM-EDS) was carried out with a field-emission scanning electron microscope (FEI Quanta-250) equipped with an Oxford Aztec energy-dispersive X-ray analysis system and a light-element X-ray detector. The nanopowder from the CuPt/Cu surface was scratched for preparing the transmission electron microscopy (TEM) analysis samples, and it was then dispersed in ethanol and ultrasonicated for 5 min, followed by drop-casting on the grid. Aberration-corrected scanning transmission electron microscopy (STEM) images and EDS mappings were taken with a Titan Themis 300 probe corrected transmission electron microscope equipped with a Super-X EDS detector. All the CuM samples were temporarily stored under inert gas before characterizations, in order to avoid any possible oxidation in air.

2.5.2. Determination of the Roughness Factor. Surface roughness factors for the electrodes relative to the copper foam were determined by comparing their double-layer capacitances ($C_{\rm dl}$). Cyclic voltammetry (CV) was performed in a three-electrode, one-compartment electrochemical cell with 1.0 M KOH without stirring. CV was conducted in the potential regions where no Faradaic processes occurred, and the difference in geometric current density (Δj) was plotted against different CV scan rates ($20-200 \text{ my s}^{-1}$).

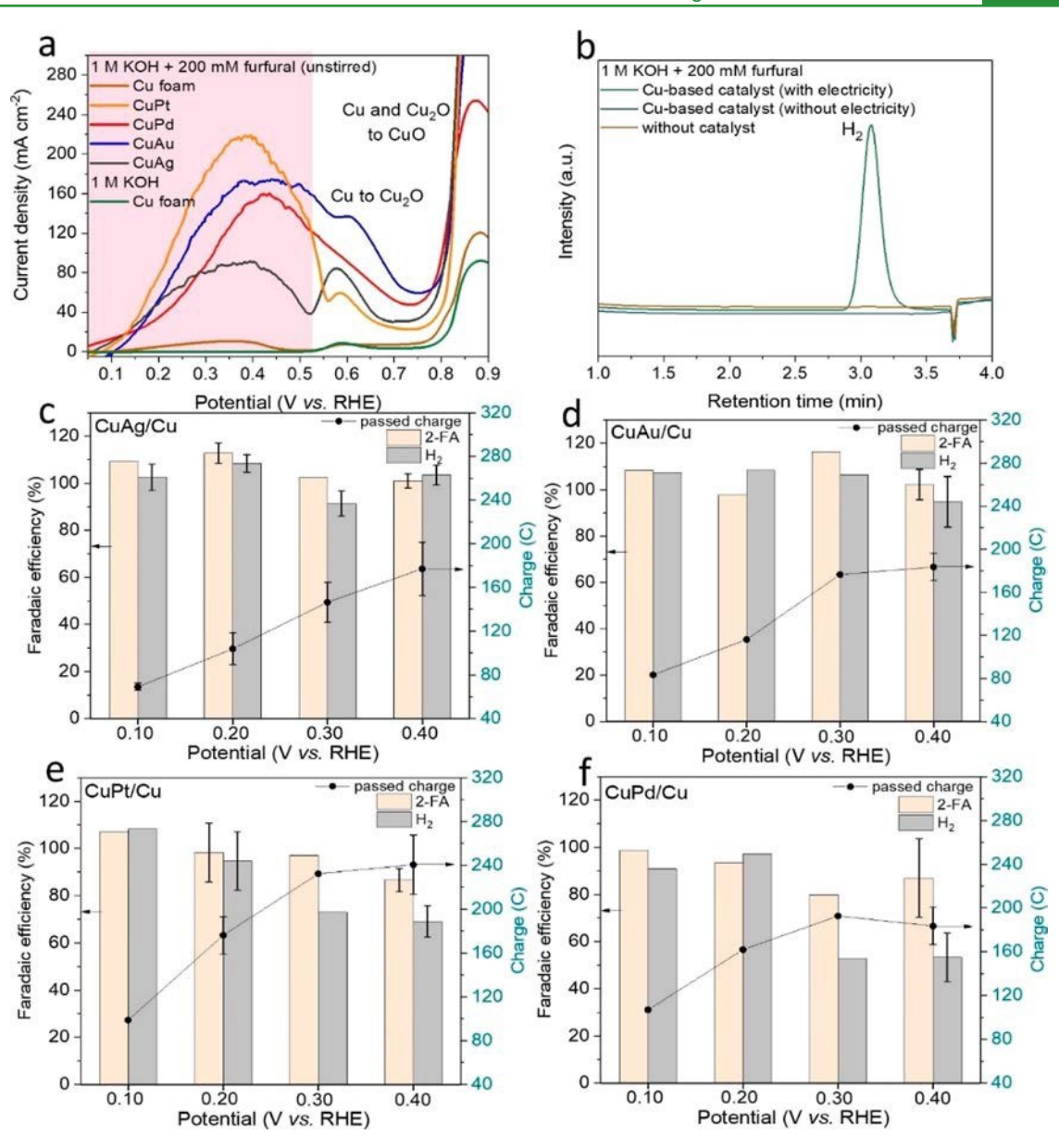


Figure 2. EOD performance on Cu-based bimetallic catalysts in the H-type cell. (a) LSV (2nd cycle) on Cu-based electrodes, including the Cu foam and CuM/Cu (M = Ag, Au, Pt, Pd), with or without 200 mM furfural in 1.0 M KOH electrolyte. (b) Online GC to detect H_2 from EOD under different experimental conditions. The retention time of H_2 was around 3 min. (c-f) Faradaic efficiency and passed charge for half-hour electrolysis on different electrodes: CuAg/Cu, CuAu/Cu, CuPt/Cu, and CuPd/Cu. The electrolyte was 200 mM furfural in 1.0 M KOH.

3. RESULTS AND DISCUSSION

3.1. Catalyst Synthesis and Morphology Characterizations. The bimetallic Cu—M catalysts (M = Ag, Au, Pd, and Pt) were prepared through a galvanic replacement method (Figure 1a). A pre-cleaned Cu foam was immersed in the precursor solutions of metal M under sonication to form CuM/Cu bimetals. Figure 1 shows the synthesis and characterization results of the CuPt/Cu electrode. The control samples, including CuAg/Cu, CuAu/Cu, and CuPd/Cu, were also prepared, characterized, and evaluated, whose details are shown in Figures S1—S8.

SEM images (Figure 1b,e) show the morphology transformation from a smooth Cu surface to a highly rough, nanosized surface after galvanic replacement under sonication. SEM-EDS analysis (Figures S1—S4) show the homogeneous distribution of M atoms on the Cu foam and a considerable

amount of oxygen associated with Cu, indicating the formation of copper oxides on the surface. Double-layer capacitance ($C_{\rm dl}$) was further measured to assess the roughness of each Cu-M material and then normalized to the plain Cu foam. Figures S5-S8 indeed suggest a significant increase in the roughness factor (RF) in four kinds of Cu-M bimetals: CuPt/Cu (4.75 \pm 0.18), CuAg/Cu (4.76 \pm 0.88), CuPd/Cu (13.1), and CuAu/Cu (22.3). These RF values can be applied to normalize the geometric current density and compare intrinsic activities among different bimetals (details shown in the next section). XRD, XPS, and high-resolution transmission electron microscopy (HR-TEM) were further carried out to analyze the crystallographic structure and electronic properties of the bimetallic catalysts. XRD analysis on CuPt/Cu suggest the presence of polycrystalline Cu and Cu₂O (Figure 1c). A minor intensity of the CuCl phase originates from incorporating chloride in the HPtCl₄ precursor into Cu. The slight peak

shifts on Cu₂O to lower degrees indicate the formation of Cu-Pt alloys, and the disappearance of Pt peaks is probably because of its alloying with Cu.^{28,29} Furthermore, a dominating peak was observed in the deconvoluted Cu 2p_{3/2} spectra from XPS at the binding energy of 932.6 eV (Figure S5e), representing the signals of Cu(0)/Cu₂O.³⁰ Two minor peaks at 933.6 and 934.8 eV correspond to CuO and Cu(OH)2, respectively.³⁰ Auger electron spectroscopy (AES) spectra of Cu LM with a kinetic energy peak at 916.4 eV further suggest that the surface is dominated by Cu₂O species (Figure 1d). Pt 4f spectra are undiscernible from XPS owing to their overlapping with the Cu 3p signal and the much stronger intensity of Cu 3p than that of Pt 4f. High-resolution STEM (HR-STEM) images show the lattice spacing of Pt, in line with the lattice spacing calculated from the fast Fourier transform (FFT) (Figure 1f,g). High-angle annular dark-field STEM (HAADF-STEM)-EDS elemental mapping further suggests the uniform dispersion of Pt on the Cu substrate (Figure 1h).

Similar characterizations were carried out in other bimetallic catalysts (see details in Supporting Information Figures S6-S8). XRD analysis suggests the co-existence of Cu, M (i.e., Ag, Au, or Pd), and Cu₂O phases in all samples. The much broader peaks of M than Cu indicate that the M domains/crystallites are small. No evidence of alloy formation was observed in the CuAg/Cu sample because of nearly no shift in Cu diffraction peaks (Figure S6d), which agreed well with our previous observations. 10 The appearance of peak shoulders or significant skews to the right in CuAu/Cu (Figure S7d) and CuPd/Cu (Figure S8d) indicate the incorporation of Au/Pd into Cu domains and the formation of alloys. The observation of alloys on CuPd, CuAu, and CuPt but not on CuAg is due to their more favorable mixability between two metal atoms, which is supported by the phase diagram of Cu-based alloys.31-34 In addition, similar to CuPt/Cu, XPS analysis of all bimetals show the Cu₂O-dominated surfaces and that M exists in its metallic chemical state.

The above characterization results suggest that the galvanic replacement methods indeed etched and oxidized the Cu surface, resulting in a significant increase of the surface area and a well dispersion of small domains of metal M on the Cu₂O-rich surface. In addition to the thermodynamic driving force between Cu and M, we found that the synthesis condition of sonication is also crucial to increasing substrate surface areas. The synthesis of highly rough bimetals reported herein has simplified preparation procedures as compared to previous works:^{35–39} in those cases, a high-surface-area Cu substrate was first synthesized by various methods (*e.g.*, electrodeposition, electroanodizing, sputtering), followed by the galvanic replacement treatment in a precursor solution for placement in a certain time period without sonication.

3.2. Electrocatalytic EOD Performance. The EOD

performance (Scheme 1, RXN 1) on CuM/Cu catalysts was investigated in a standard three-electrode H-type cell. The assynthesized CuM/Cu was first held at $-0.1~\rm V_{RHE}$ for 3 min to reduce surface Cu₂O to metallic Cu in the furfural-containing electrolyte. LSV was performed in 1.0 M KOH with and without furfural. As shown in Figure 2a, the EOD reaction with apparent current densities is mainly dominated in the potential range of $0.1-0.5~\rm V_{RHE}$ on five Cu-based electrodes. A further positive shift of the anodic potential would oxidize Cu to its oxides and trigger the electrocatalytic oxidation (ECO) of furfural without H₂ evolution (Scheme 1, RXN 2).¹⁰ The current density profiles (without stirring of the anolyte) show

the EOD activity on different bimetallic electrodes, following the order of CuPt/Cu > CuAu/Cu > CuPd/Cu > CuAg/Cu, much higher than that of the Cu foam (Figure 2a).

EOD activity on CuM/Cu electrodes was further tested under static electrolysis conditions at different anodic potentials (Figure 2b-e). H₂ was quantified by online gas chromatography (GC, Figure 2b), and 2-FA and furfural alcohol were quantified by offline high-performance liquid chromatography (HPLC). The FEs of 2-FA and H₂ are defined as the moles of 2-FA or 2 times of moles of H₂ produced divided by the total moles of electrons applied. It is noted that the reported FE of 2-FA from the EOD pathway was calculated after subtracting 2-FA co-produced from the non-Faradaic Cannizzaro reaction (quantified from the amount of produced furfuryl alcohol, Scheme 1, RXN 4). A control experiment showed that furfuryl alcohol is unreactive for the EOD pathway in H₂ evolution (Figure S9). Table S1 shows a detailed calculation of FE of 2-FA from the EOD pathway. With 30 min electrolysis at different potentials, we obtained ~100% FEs of both 2-FA and H₂ on CuAg/Cu and CuAu/Cu electrodes in the potential range of 0.1-0.4 V_{RHE}. The passed charge (Figure 2c,d, right y-axis) increased from 0.1 to 0.4 V_{RHE}, consistent with the LSV trend. These results suggested that EOD is the dominant, sole Faradaic reaction under this potential range.

The EOD activity on CuPt/Cu and CuPd/Cu presents a different trend in terms of the FEs of product (Figure 2e,f). At 0.1-0.2 V_{RHE}, we observed >95% FEs of 2-FA and H₂, approaching that on CuAg/Cu and CuAu/Cu electrodes. When the anodic potential $\geq 0.3 \text{ V}_{\text{RHE}}$, we observed a decrease in the FEs of 2-FA and H₂. The H₂ FE dropped to \sim 70% and ~50% for CuPt/Cu and CuPd/Cu catalysts, respectively, likely due to a hydrogen spillover pathway (Figure S10). That is, the C-H cleavage along with the aldehyde oxidation to acid occurred on Cu sites; instead of producing H2 through a Tafel step for self-coupling of adsorbed H (H*) on Cu, certain H* would spill over to the adjacent noble metal sites for its conversion toward H+ through a reverse Volmer step. The detailed mechanism will be studied in our future work. Additional control experiments (Figure S11a) on commercial nanoparticles (Pd/C, Pt/C, Au/C, and Ag/C) confirmed the favorable hydrogen oxidation reaction (HOR) toward H+ on noble metals (i.e., Pd/C and Pt/C) even under low anodic potentials (e.g., 0-0.4 V_{REH}), while HOR was suppressed on Ag/C and Au/C, in line with the FE trend of EOD on those four Cu-M bimetals and the proposed hydrogen spillover mechanism. The oxidation of H* to H+ can be minimized by negatively shifting the anodic potential, in accordance with our experimental observation of high H₂ FE (>95%) for EOD on CuPt/Cu and CuPd/Cu at 0.1 and 0.2 V_{RHE}, respectively. Besides, this H* oxidation to H⁺ on noble metal sites mainly occurred through the surface diffusion of H* at local regions, rather than the reabsorption of the EOD-produced H₂ for its further oxidation through HOR. This can be supported by the control experiment of the inactive nature of Cu-M catalysts (e.g., CuPt/Cu) for HOR, particularly in the potential range of 0-0.4 V_{REH} with excessive H₂ supply (100 mL min⁻¹, Figure

Additionally, during EOD, the dynamic surface reconstruction rearranged the lattice of the Cu-M catalysts and maintained the high-surface-area porous structure. SEM images (Figure S12) show a significant morphology transformation after a half-hour EOD at $0.2\,V_{RHE}$. For instance, the

surface morphology of the CuAu/Cu and CuPd/Cu catalysts changed from spherical nanoparticles to nanosheets. Interestingly, post-electrolysis characterizations showed that those electrochemically induced surface reconstructions caused an increase in their surface roughness (Figure S12), which could be beneficial for stabling the EOD performance (details are discussed in the last section). These dynamic surface morphology changes are driven by the significant mobility of Cu and M at room temperature and the anodic biasing during EOD. A similar observation of dynamic surface reconstruction of catalysts with an enhancement in electrocatalytic activity has been observed in recent works on different electrochemical reactions, such as NO -to-NH, 30,40 different electrochemical reactions, such as NO -to-NH, 30,40 different electrochemical

3.3. Strong Synergistic Effects on the CuPt/Cu Catalyst. Despite a slight H_2 FE decrease on the CuPt/Cu catalyst, especially at more positive potentials, the key advantage of CuPt/Cu is its strong synergistic effect between Cu and Pt for EOD. In terms of j_{AH_2} , CuPt/Cu showed the highest values of 239 and 357 mA cm at 0.2 and 0.4 V_{RHE} , respectively, among all four CuM/Cu catalysts (Figure 3 right

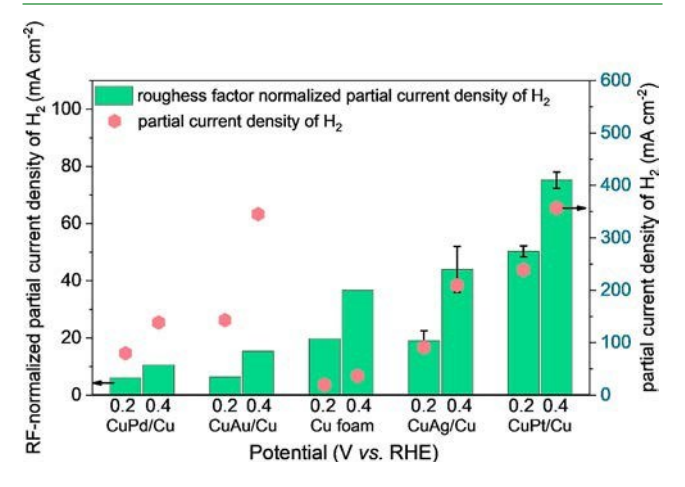


Figure 3. Comparison of the roughness factor (RF)-normalized partial current density of H_2 and partial current density of H_2 among different Cu-based bimetallic catalysts.

y-axis). It is worth mentioning that we accounted for the partial current density at the early stage of steady-state EOD (*i.e.*, 3 min) to avoid the mass transport limitation, which resulted from the furfural consumption during electrolysis in the batch reactor (15 mL) that caused a gradual decrease in the current density (Figure S13). Moreover, we carried out electrokinetic studies and fitted the apparent activation energy (E_a) on the CuPt/Cu electrode to be 53.8 \pm 8.7 kJ mol⁻¹ at 0.1 V_{RHE}, by changing the temperature from 25 to 43 °C (Figure S14).

To compare the intrinsic activities of the catalysts considering their distinct surface areas, we normalized $j_{\rm A\,H^{-}}$ to the roughness factor (*i.e.*, RF- $j_{\rm A\,H_2}$) (Figure 3 left y-axis). Importantly, CuPt/Cu with the lowest RF (*i.e.*, 4.75 \pm 0.18) displayed the highest RF- $j_{\rm A^{-}\,H_2}$ at both 0.2 and 0.4 V_{RHE}, following the order of CuPt/Cu > CuAg/Cu > Cu foam > CuAu/Cu > CuPd/Cu. Supported by our previous DFT calculation of the EOD pathway on different metals (Pt, Au, and Cu), we proposed that the strong synergistic effects on the CuPt/Cu catalyst take advantage of the facile interaction between furfural and Pt sites, considering its binding energy on Pt of -2.11 eV as compared to that on Cu (-1.06 eV) and

other metals (e.g., Au, -0.96 eV), and the favorable C–H cleavage on Cu sites as opposed to that on Pt (limited by CO poisoning) and Au (limited by slow C–H activation). Besides, CuAu/Cu showed a high absolute $j_{\text{A-H}_2}$ because of its highest surface roughness (RF = 22.3) among four bimetallic catalysts. However, the RF- $j_{\text{A-H}_2}$ on CuAu and CuPd is greatly

minimized and lower than that on the Cu foam, resulting from the inactive EOD property on Au and Pd. ¹⁰ In such a manner, the incorporation of Au and Pd occupied surface Cu sites, leading to a decrease in EOD performance and lower than that on a monometallic Cu surface (*i.e.*, Cu foam). In contrast, CuAg/Cu exhibited a second high RF-*j* because

of the catalytic EOD activity on both Cu and Ag $\hat{\mathbf{m}}_{\mathrm{Catal}}^{\mathrm{Ha}}$, but the lower $\hat{\mathbf{j}}_{\mathrm{AH}_2}$ and RF- $\hat{\mathbf{j}}_{\mathrm{AH}_2}$ on CuAg than that on CuPt

could be due to the minimal synergistic effect between Cu and Ag. It is worth noting that the experimental screening of different metals for EOD was also reported in our previous work. 10 These results clearly demonstrated that the superior EOD performance on CuPt/Cu is not only from its high surface area but also from the synergistic effects of Cu and Pt with higher intrinsic activity. The EOD performance on the CuPt/Cu anode has outperformed the recent publications for aldehyde oxidation with H₂ evolution (Table S1).

3.4. Bipolar H₂ Production Flow Systems. Based on the facile EOD kinetics on Cu-based electrodes and the optimized bimetal combinations, we implemented an MEA-based flow cell for bipolar H₂ production (Figure 4a,b). The MEA contained a Pt/C cathode, an anion exchange membrane (AEM, Tokuyama A201), and a CuM/Cu anode in a zero-gap configuration. 1.0 M KOH with and without furfural were used as the anolyte and the catholyte, respectively, each with a volume of 250 mL.

LSV measurement of the HER-EOD paired bipolar H₂ production displayed ultra-low cell voltages (Figure 4c). At the current density of 100 mA cm⁻², the cell voltages were below 0.3 V for all four Cu-based bimetals, following the order of CuPt/Cu < CuAu/Cu < CuPd/Cu < CuAg/Cu. At steadystate electrolysis at 0.6 V (Figure 4d), the $j_{\rm A~H_2}$ attained 498 mA cm⁻² on the CuPt/Cu electrode, with the anodic H₂ FE of 80.5%. These high performances benefit from the facile EOD kinetics on Cu-based bimetals and the largely facilitated mass transport by flow cell implementation. Our observed ultra-low cell voltages and industrially relevant current densities for bipolar H₂ production (Supporting Information Movie S1) with valuable 2-FA co-production have outperformed recently reported values.9 Besides, our work's cell voltages and current densities are also superior to conventional ECO-HER paired systems (e.g., organic ECO-HER,42-47 inorganic ECO-HER^{48–50}) for cathodic H₂ production: in those cases, the cell voltages are >1.0 V with current densities <100 mA cm⁻². Finally, we performed durability tests for bipolar H₂ production with these bimetallic anodes in MEA-based flow

electrolyzers (Figure S15). After 5 successive cycles of 1 h electrolysis (i.e., refreshing catholyte at 1 h interval) at the cell voltage of 0.4 V, CuAu/Cu showed the best durability with only a 4.5% performance decrease. Indeed, we noticed a slight increase in activity on CuAu/Cu (10.7%) and CuAg/Cu (0.9%) during the second 1 h cycle, benefiting from the surface reconstruction-induced roughness increase. We observed relatively poor durability of CuPt/Cu and CuPd/Cu electrodes, which are not because of the surface roughness decrease

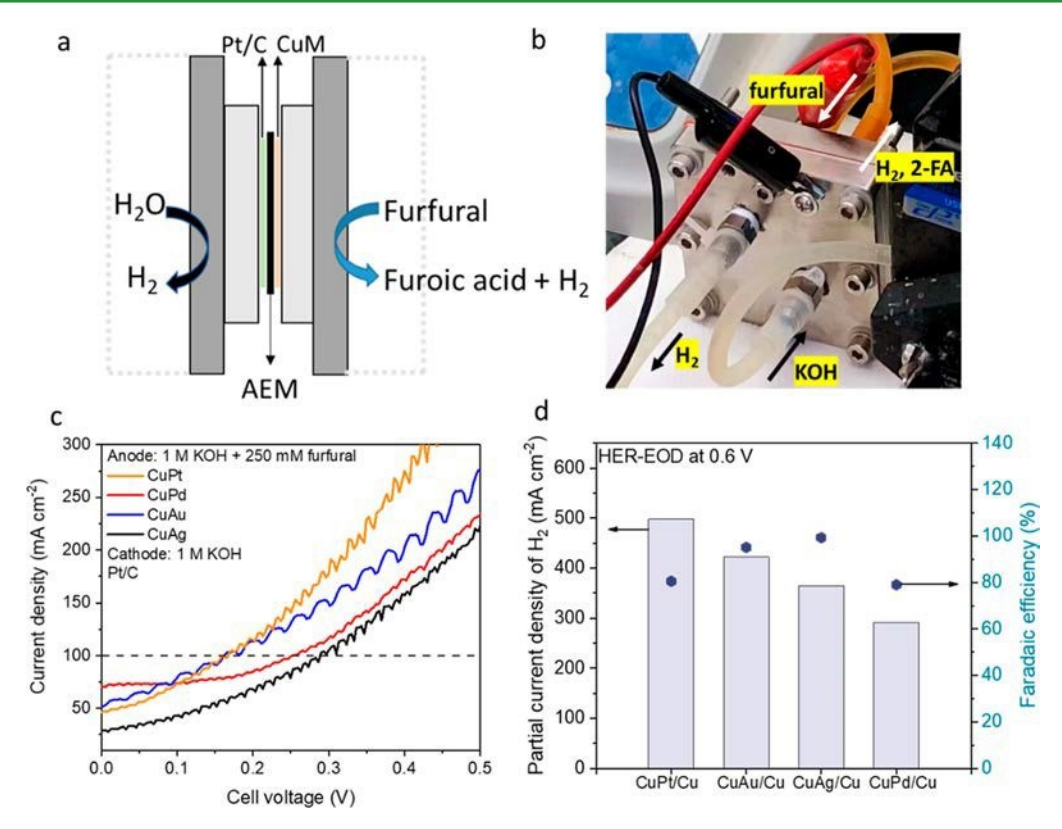


Figure 4. Bipolar H_2 production in the MEA-based flow cells. (a) Scheme and (b) photograph of the reactor setup. (c) Linear sweep voltammograms of bipolar H_2 production with the Pt/C cathode and Cu-based bimetallic anodes. (d) Partial current density of anodic H_2 and its FE at the cell voltage of 0.6 V. 250 mM furfural in 1.0 M KOH was used as the anolyte and 1.0 M KOH was used as the catholyte. The electrolyte volume was 250 mL.

since RF only showed a slight change after 5 h electrolysis (Figures S16 and S17). The primary reason for catalyst deactivation could be due to the complete phase transformation of metallic Cu toward Cu(OH)₂ (as supported by XPS Cu 2p and O 1s spectra in Figures S16 and S17), which is not the reactive phase for EOD.¹⁰ In the meantime, a small amount of CO-like intermediates generated from furfural oxidation may also poison the Pt/Pd catalysts. Developing more durable Cu-based electrocatalysts, especially under harsh electrolytic conditions of high alkalinity and anodic biasing,⁵¹ remains a challenge that needs to be addressed in future studies.

4. CONCLUSIONS

In summary, this work reported a simple galvanic replacement method to prepare Cu-based bimetallic catalysts for EOD toward practical rate, bipolar H₂ production. Taking advantage of the thermodynamic driving force between Cu and other metals (M), the Cu foam surface can be etched and oxidized, resulting in a significant increase in the surface area and well dispersion of M. In particular, the CuPt/Cu catalyst has achieved j_{A-H_2} values of 357 mA cm⁻² at 0.4 V_{RHE} in the batch reactor and 498 mA cm at the cell voltage of 0.6 V in the MEA-based flow electrolyzer. Our work presented ultra-low cell voltages and industrial-level current densities toward bipolar H₂ production in a sustainable manner, with the coproduction of valuable carboxylic acid. Further development of more durable Cu-based catalysts, exploration of alternative large-scale aldehyde feedstocks, and demonstration of costeffective processes will bring exciting new opportunities for

distributed manufacturing of green hydrogen and carbon chemicals with low energy consumption and low carbon footprint in the future.



ASSOCIATED CONTENT

Supporting Information

The Supporting Information is available free of charge at https://pubs.acs.org/doi/10.1021/acsami.3c06783.

Physical characterization (SEM, EDS, XRD, and XPS) of Cu-based catalysts, electrochemical tests of Cu-based catalysts in the H-type cell and flow cell, durability test, electrokinetic study, control experiments, and comparison of EOD performance on various electrodes (PDF)

Bipolar H₂ flow cell (MP4)



AUTHOR INFORMATION

Corresponding Author

Wenzhen Li — Department of Chemical and Biological Engineering, Iowa State University, Ames, Iowa 50011,

United States; orcid.org/0000-0002-1020-5187; Email: wzli@iastate.edu

Authors

Hengzhou Liu — Department of Chemical and Biological Engineering, Iowa State University, Ames, Iowa 50011, United States

Jiaqi Yu — Department of Chemistry, Iowa State University, Ames, Iowa 50011, United States

- Yifu Chen Department of Chemical and Biological Engineering, Iowa State University, Ames, Iowa 50011, United States; ⊙ orcid.org/0000-0001-7877-686X
- Jungkuk Lee Department of Chemical and Biological Engineering, Iowa State University, Ames, Iowa 50011, United States
- Wenyu Huang − Department of Chemistry, Iowa State University, Ames, Iowa 50011, United States; orcid.org/0000-0003-2327-7259

Complete contact information is available at: https://pubs.acs.org/10.1021/acsami.3c06783

Notes

The authors declare no competing financial interest.

A

ACKNOWLEDGMENTS

This work was supported by the National Science Foundation under grant no. CBET-1947435 and USDA NIFA (2021-67021-34650). W.L. is grateful to his Herbert L. Stiles Faculty Fellowship, the IEC competitive fund (20-IEC-019), and his ISU-PIRI grant. We thank Drs. Dapeng Jing, Warren E. Straszheim, and Carolina Salvati for their assistance with XPS, SEM-EDS, and XRD measurements. We are grateful for helpful discussion with Prof. Michael Janik, and Dr. Naveen Agrawal on DFT computation of electrochemical oxidation of aldehydes; and with Mohammad Albloushi on some electrochemical tests. We thank Prof. Emily Smith and Mohammad Khalid Ibne Walid for their fruitful discussion of catalyst characterizations.

R

REFERENCES

- (1) Carmo, M.; Fritz, D. L.; Mergel, J.; Stolten, D. A comprehensive review on PEM water electrolysis. *Int. J. Hydrogen Energy* 2013, *38*, 4901–4934.
- (2) Holladay, J. D.; Hu, J.; King, D. L.; Wang, Y. An overview of hydrogen production technologies. *Catal. Today* 2009, 139, 244–260.
- (3) Ursua, A.; Gandia, L. M.; Sanchis, P. Hydrogen production from water electrolysis: current status and future trends. *Proc. IEEE* 2012, 100, 410–426.
- (4) Zeng, K.; Zhang, D. Recent progress in alkaline water electrolysis for hydrogen production and applications. *Prog. Energy Combust. Sci.* 2010, *36*, 307–326.
- (5) You, B.; Sun, Y. Innovative strategies for electrocatalytic water splitting. *Acc. Chem. Res.* 2018, *51*, 1571–1580.
- (6) Rausch, B.; Symes, M. D.; Chisholm, G.; Cronin, L. Decoupled catalytic hydrogen evolution from a molecular metal oxide redox mediator in water splitting. *Science* 2014, 345, 1326–1330.
- (7) You, B.; Liu, X.; Jiang, N.; Sun, Y. A general strategy for decoupled hydrogen production from water splitting by integrating oxidative biomass valorization. *J. Am. Chem. Soc.* 2016, *138*, 13639—13646.
- (8) You, B.; Liu, X.; Liu, X.; Sun, Y. Efficient H₂ evolution coupled with oxidative refining of alcohols via a hierarchically porous nickel bifunctional electrocatalyst. *ACS Catal.* 2017, 7, 4564–4570.
- (9) Wang, T.; Tao, L.; Zhu, X.; Chen, C.; Chen, W.; Du, S.; Zhou, Y.; Zhou, B.; Wang, D.; Xie, C.; et al. Combined anodic and cathodic hydrogen production from aldehyde oxidation and hydrogen evolution reaction. *Nat. Catal.* 2022, *5*, 66–73.
- (10) Liu, H.; Agrawal, N.; Ganguly, A.; Chen, Y.; Lee, J.; Yu, J.; Huang, W.; Mba Wright, M.; Janik, M.; Li, W. Ultra-Low Voltage Bipolar Hydrogen Production from Biomass-Derived Aldehydes and Water in Membrane-Less Electrolyzers. *Energy Environ. Sci.* 2022, 15, 4175–4189.

- (11) Nam, D.-H.; Taitt, B. J.; Choi, K.-S. Copper-based catalytic anodes to produce 2, 5-furandicarboxylic acid, a biomass-derived alternative to terephthalic acid. *ACS Catal.* 2018, 8, 1197–1206.
- (12) Bender, M. T.; Lam, Y. C.; Hammes-Schiffer, S.; Choi, K.-S. Unraveling two pathways for electrochemical alcohol and aldehyde oxidation on NiOOH. *J. Am. Chem. Soc.* 2020, 142, 21538–21547.
- (13) Zhang, Y.; Zhou, B.; Wei, Z.; Zhou, W.; Wang, D.; Tian, J.; Wang, T.; Zhao, S.; Liu, J.; Tao, L.; et al. Coupling Glucose-Assisted Cu (I)/Cu (II) Redox with Electrochemical Hydrogen Production. *Adv. Mater.* 2021, 33, 2104791.
- (14) Zhou, B.; Zhang, Y.; Wang, T.; Zhou, W.; Liu, J.; Zou, Y.; Tao, L.; Lu, Y.; Wang, S. Room-temperature chemical looping hydrogen production mediated by electrochemically induced heterogeneous Cu (I)/Cu (II) redox. *Chem Catal.* 2021, 1, 1493–1504.
- (15) Zhang, S.; Ma, Y.; Zhang, H.; Zhou, X.; Chen, X.; Qu, Y. Additive-Free Robust H2 Production from H2O and DMF by Dehydrogenation Catalyzed by Cu/Cu₂O Formed In Situ. *Angew. Chem., Int. Ed.* 2017, 56, 8245–8249.
- (16) Liang, S.; Chen, S.; Guo, Z.; Lan, Z.; Kobayashi, H.; Yan, X.; Li, R. In situ generated electron-deficient metallic copper as the catalytically active site for enhanced hydrogen production from alkaline formaldehyde solution. *Catal. Sci. Technol.* 2019, 9, 5292–5300
- (17) Ashby, E. C.; Doctorovich, F.; Liotta, C. L.; Neumann, H. M.; Barefield, E. K.; Konda, A.; Zhang, K.; Hurley, J.; Siemer, D. D. Concerning the formation of hydrogen in nuclear waste. Quantitative generation of hydrogen via a Cannizzaro intermediate. *J. Am. Chem. Soc.* 1993, 115, 1171–1173.
- (18) Kapoor, S.; Barnabas, F. A.; Sauer, M. C.; Meisel, D.; Jonah, C. D. Kinetics of Hydrogen Formation from Formaldehyde in Basic Aqueous Solutions. *J. Phys. Chem.* 1995, *99*, 6857–6863.
- (19) Chen, X.; Zhang, H.; Xia, Z.; Zhang, S.; Ma, Y. Base-free hydrogen generation from formaldehyde and water catalyzed by copper nanoparticles embedded on carbon sheets. *Catal. Sci. Technol.* 2019, 9, 783–788.
- (20) Heim, L. E.; Schlörer, N. E.; Choi, J.-H.; Prechtl, M. H. Selective and mild hydrogen production using water and formaldehyde. *Nat. Commun.* 2014, 5, 3621.
- (21) Trincado, M.; Sinha, V.; Rodriguez-Lugo, R. E.; Pribanic, B.; de Bruin, B.; Grützmacher, H. Homogeneously catalysed conversion of aqueous formaldehyde to H₂ and carbonate. *Nat. Commun.* 2017, 8, 14990.
- (22) Wang, L.; Ertem, M. Z.; Kanega, R.; Murata, K.; Szalda, D. J.; Muckerman, J. T.; Fujita, E.; Himeda, Y. Additive-free ruthenium-catalyzed hydrogen production from aqueous formaldehyde with high efficiency and selectivity. *ACS Catal.* 2018, *8*, 8600–8605.
- (23) Kar, S.; Zhou, Q.-Q.; Ben-David, Y.; Milstein, D. Catalytic Furfural/5-Hydroxymethyl Furfural Oxidation to Furoic Acid/Furan-2, 5-dicarboxylic Acid with H₂ Production Using Alkaline Water as the Formal Oxidant. *J. Am. Chem. Soc.* 2022, 144, 1288–1295.
- (24) Lange, J. P.; van der Heide, E.; van Buijtenen, J.; Price, R. Furfural promising platform for lignocellulosic biofuels. *Chem-SusChem* 2012, 5, 150–166.
- (25) Mariscal, R.; Maireles-Torres, P.; Ojeda, M.; Sádaba, I.; López Granados, M. Furfural: a renewable and versatile platform molecule for the synthesis of chemicals and fuels. *Energy Environ. Sci.* 2016, 9, 1144–1189.
- (26) Zhang, Z.; Lees, E. W.; Habibzadeh, F.; Salvatore, D. A.; Ren, S.; Simpson, G. L.; Wheeler, D. G.; Liu, A.; Berlinguette, C. P. Porous metal electrodes enable efficient electrolysis of carbon capture solutions. *Energy Environ. Sci.* 2022, *15*, 705–713.
- (27) Song, F.; Zhang, T.; Zhou, D.; Sun, P.; Lu, Z.; Bian, H.; Dang, J.; Gao, H.; Qian, Y.; Li, W.; et al. Charge Transfer of Interfacial Catalysts for Hydrogen Energy. *ACS Mater. Lett.* 2022, 4, 967–977.
- (28) Zhang, X.; Cui, G.; Feng, H.; Chen, L.; Wang, H.; Wang, B.; Zhang, X.; Zheng, L.; Hong, S.; Wei, M. Platinum—copper single atom alloy catalysts with high performance towards glycerol hydrogenolysis. *Nat. Commun.* 2019, *10*, 5812.

- (29) Clark, E. L.; Hahn, C.; Jaramillo, T. F.; Bell, A. T. Electrochemical CO₂ reduction over compressively strained CuAg surface alloys with enhanced multi-carbon oxygenate selectivity. *J. Am. Chem. Soc.* 2017, 139, 15848–15857.
- (30) Biesinger, M. C. Advanced analysis of copper X-ray photoelectron spectra. Surf. Interface Anal. 2017, 49, 1325–1334.
- (31) Popov, A.; Shubin, Y. V.; Plyusnin, P.; Sharafutdinov, M.; Korenev, S. Experimental redetermination of the Cu-Pd phase diagram. *J. Alloys Compd.* 2019, 777, 204–212.
- (32) Kawecki, A.; Knych, T.; Sieja-Smaga, E.; Mamala, A.; Kwasniewski, P.; Kiesiewicz, G.; Smyrak, B.; Pacewicz, A. Fabrication, Properties and Microstructures of High Strength and High Conductivity Copper-Silver Wires / Otrzymywanie Oraz Własnosci I Mikrostruktura Wysokowytrzymałych I Wysoko Przewodzacych Drutów Ze Stopow Cu-Ag. Arch. Metall. Mater. 2012, 57, 1261–1270.
- (33) Abe, T.; Sundman, B.; Onodera, H. Thermodynamic assessment of the Cu- Pt system. *J. Phase Equilibria Diffus*. 2006, 27, 5–13.
- (34) Ravi, R.; Paul, A. Diffusion mechanism in the gold-copper system. *J. Mater. Sci. Mater.* 2012, 23, 2152–2156.
- (35) Chen, F.-Y.; Wu, Z.-Y.; Gupta, S.; Rivera, D. J.; Lambeets, S. V.; Pecaut, S.; Kim, J. Y. T.; Zhu, P.; Finfrock, Y. Z.; Meira, D. M.; King, G.; Gao, G.; Xu, W.; Cullen, D. A.; Zhou, H.; Han, Y.; Perea, D. E.; Muhich, C. L.; Wang, H. T. Efficient conversion of low-concentration nitrate sources into ammonia on a Ru-dispersed Cu nanowire electrocatalyst. *Nat. Nanotechnol.* 2022, 17, 759—767.
- (36) Wang, X.; Ou, P.; Ozden, A.; Hung, S.-F.; Tam, J.; Gabardo, C. M.; Howe, J. Y.; Sisler, J.; Bertens, K.; García de Arquer, F. P.; et al. Efficient electrosynthesis of n-propanol from carbon monoxide using a Ag–Ru–Cu catalyst. *Nat. Energy* 2022, 7, 170–176.
- (37) Lv, X.; Shang, L.; Zhou, S.; Li, S.; Wang, Y.; Wang, Z.; Sham, T. K.; Peng, C.; Zheng, G. Electron-deficient Cu sites on Cu3Ag1 catalyst promoting CO₂ electroreduction to alcohols. *Adv. Energy Mater.* 2020, 10, 2001987.
- (38) Gao, J.; Zhang, H.; Guo, X.; Luo, J.; Zakeeruddin, S. M.; Ren, D.; Grätzel, M. Selective C–C coupling in carbon dioxide electroreduction via efficient spillover of intermediates as supported by operando Raman spectroscopy. *J. Am. Chem. Soc.* 2019, 141, 18704–18714.
- (39) Sanghez de Luna, G.; Ho, P. H.; Sacco, A.; Hernández, S.; Velasco-Vélez, J.-J. s.; Ospitali, F.; Paglianti, A.; Albonetti, S.; Fornasari, G.; Benito, P. AgCu Bimetallic Electrocatalysts for the Reduction of Biomass-Derived Compounds. *ACS Appl. Mater. Interfaces* 2021, 13, 23675–23688.
- (40) Li, S.; Ma, P.; Gao, C.; Liu, L.; Wang, X.; Shakouri, M.; Chernikov, R.; Wang, K.; Liu, D.; Ma, R.; et al. Reconstruction-induced NiCu-based Catalysts towards Paired Electrochemical Refining. *Energy Environ. Sci.* 2022, *15*, 3004–3014.
- (41) Zhao, C.-X.; Liu, J.-N.; Wang, C.; Wang, J.; Song, L.; Li, B.-Q.; Zhang, Q. An anionic regulation mechanism for the structural reconstruction of sulfide electrocatalysts under oxygen evolution conditions. *Energy Environ. Sci.* 2022, *15*, 3257–3264.
- (42) Yang, G.; Jiao, Y.; Yan, H.; Xie, Y.; Wu, A.; Dong, X.; Guo, D.; Tian, C.; Fu, H. Interfacial engineering of MoO2-FeP heterojunction for highly efficient hydrogen evolution coupled with biomass electrooxidation. *Adv. Mater.* 2020, 32, 2000455.
- (43) Wang, L.; Zhu, Y.; Wen, Y.; Li, S.; Cui, C.; Ni, F.; Liu, Y.; Lin, H.; Li, Y.; Peng, H.; et al. Regulating the local charge distribution of Ni active sites for the urea oxidation reaction. *Angew. Chem.* 2021, 133, 10671–10676.
- (44) Zhang, Y.; Zhou, B.; Wei, Z.; Zhou, W.; Wang, D.; Tian, J.; Wang, T.; Zhao, S.; Liu, J.; Tao, L.; et al. Coupling Glucose-Assisted Cu (I)/Cu (II) Redox with Electrochemical Hydrogen Production. *Adv. Mater.* 2021, 33, 2104791.
- (45) Zhao, H.; Lu, D.; Wang, J.; Tu, W.; Wu, D.; Koh, S. W.; Gao, P.; Xu, Z. J.; Deng, S.; Zhou, Y.; et al. Raw biomass electroreforming coupled to green hydrogen generation. *Nat. Commun.* 2021, 12, 2008. (46) Geng, S.-K.; Zheng, Y.; Li, S.-Q.; Su, H.; Zhao, X.; Hu, J.; Shu, H.-B.; Jaroniec, M.; Chen, P.; Liu, Q.-H.; et al. Nickel ferrocyanide as

- a high-performance urea oxidation electrocatalyst. *Nat. Energy* 2021, 6, 904–912.
- (47) Liu, W.-J.; Xu, Z.; Zhao, D.; Pan, X.-Q.; Li, H.-C.; Hu, X.; Fan, Z.-Y.; Wang, W.-K.; Zhao, G.-H.; Jin, S.; et al. Efficient electrochemical production of glucaric acid and H2 via glucose electrolysis. *Nat. Commun.* 2020. 11. 265.
- (48) Qian, Q.; Zhang, J.; Li, J.; Li, Y.; Jin, X.; Zhu, Y.; Liu, Y.; Li, Z.; El-Harairy, A.; Xiao, C.; et al. Artificial heterointerfaces achieve delicate reaction kinetics towards hydrogen evolution and hydrazine oxidation catalysis. *Angew. Chem.* 2021, 133, 6049–6058.
- (49) Wang, D.; He, N.; Xiao, L.; Dong, F.; Chen, W.; Zhou, Y.; Chen, C.; Wang, S. Coupling electrocatalytic nitric oxide oxidation over carbon cloth with hydrogen evolution reaction for nitrate synthesis. *Angew. Chem.* 2021, 133, 24810–24816.
- (50) Dresp, S.; Ngo Thanh, T.; Klingenhof, M.; Bruckner, S.; Hauke, P.; Strasser, P. Efficient direct seawater electrolysers using selective alkaline NiFe-LDH as OER catalyst in asymmetric electrolyte feeds. *Energy Environ. Sci.* 2020, *13*, 1725–1729.
- (51) Liu, G.; Zheng, F.; Li, J.; Zeng, G.; Ye, Y.; Larson, D. M.; Yano, J.; Crumlin, E. J.; Ager, J. W.; Wang, L.-W.; et al. Investigation and mitigation of degradation mechanisms in Cu₂O photoelectrodes for CO₂ reduction to ethylene. *Nat. Energy* 2021, 6, 1124–1132.